Prior Computation of the Stator Current Dynamic Response for Torque Ripple Reduction in AC Motor Drives

Hemantha Kumar Ravi, Sathyanarayanan Nandagopal and Lenin Natesan Chokkalingam*

Electric Vehicles – Incubation, Testing and Research Centre, Vellore Institute of Technology, Chennai, India
E-mail: rhemantha.kumar2014@vit.ac.in; sathyanarayanan.n2014@vit.ac.in; lenin.nc@vit.ac.in
**Corresponding Author*

Received 29 January 2023; Accepted 24 November 2023;
Publication 31 January 2024

Abstract

In electric vehicles, the performance of the electric motor drive system depends on the characteristics of the control scheme applied. This paper discusses the torque ripple in an induction motor drive scheme exclusively and also proposes a new scheme to minimize it. The major cause of the torque ripple in induction motor drive is the presence of a high stator torque component (q-axis current) ripple. In the proposed scheme, the inverter is switched with the optimal duty ratio for the minimum q-axis current ripple. This leads to a decrease in q-axis current error and eventually torque ripple reduction. The distortion of the stator current waveform is also limited and gives rise

Distributed Generation & Alternative Energy Journal, Vol. 39_2, 341–368.
doi: 10.13052/dgaej2156-3306.3926

to lower total harmonic distortion (THD). The feasibility of this proposed duty ratio modulated (DRM) improved torque and flux control scheme is studied using the MATLAB/Simulink computation tool and validated through appropriate experimentation.

Keywords: Dynamic current control, duty ratio modulation, field-oriented control.

1 Introduction

Presently, AC drives have revived themselves with the recent developments in the electric vehicle industry [1–3]. Torque ripple in the motor drive system in electric vehicles causes vibration in the drive line. But torque ripple is inevitable in electric motor drives [1, 2], especially induction motor (IM) drives, because of the stator current ripple produced by the torque control schemes, while switching the inverter [1–5]. In field-oriented control (FOC) based IM drive algorithms, ripples in the stator d-q current components are reduced using various current regulation strategies [4–6]. The general block diagram of the FOC drive is shown in Figure 1. FOC stator current regulation strategies can be classified as linear and non-linear current regulators [5]. In linear current regulators, pulse width modulators (PWM) like

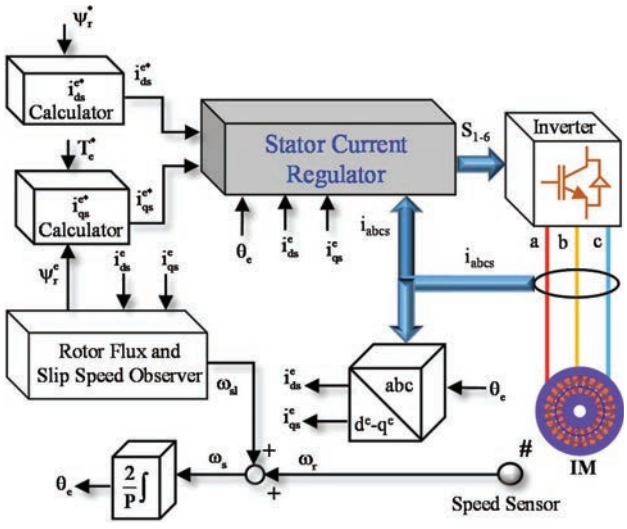

Figure 1 Field-oriented control of IM – a comprehensive block diagram.

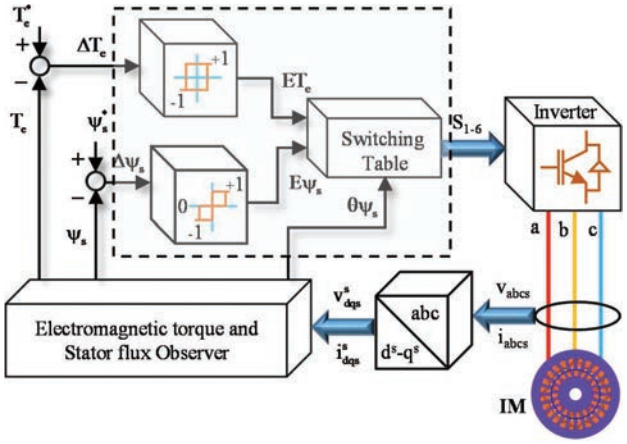

Figure 2 Block diagram of the direct torque control algorithm.

sine PWM, space vector PWM etc., are used for stator current regulation [7–15]. Whereas, non-linear regulators provide current regulation through (1) Hysteresis controllers [16–24], (2) Online optimal controllers [25–28], and (3) Soft computing controllers [29, 30]. Linear current regulators operate at a constant switching frequency and produce better stator current characteristics (balanced phase currents with lower ripple and harmonics) than non-linear regulators [5, 6]. However, non-linear controllers have certain inherent advantages such as good error tracking, simple and robust control [5, 6].

Apart from field-oriented control, the direct torque control (DTC) scheme has also been a viable solution for torque control in AC drives [31–39]. In DTC, torque and stator flux are controlled directly using a hysteresis controller-switching table based structure as shown in Figure 2. This simple control structure of DTC has led to a fast dynamic torque response [1, 2]. DTC also suffers from high torque ripple and variable switching frequency [1, 2]. This high torque ripple is because of the inappropriate selection of the control voltage vector for the torque control within the torque hysteresis band [33, 34].

The torque ripple in DTC and FOC drives has been reported to be about 18% and 11% respectively [36]. In similar drive operating conditions, the current ripple was also found to be 6.63% (DTC) and 3.86% (FOC) [36].

In 1991, Marian P. Kazmierkowski et al. introduced a non-linear FOC scheme (NLFOC) with a DTC structure as shown in Figure 3 [16, 17]. In this scheme, control voltage space vectors are selected from the switching table,

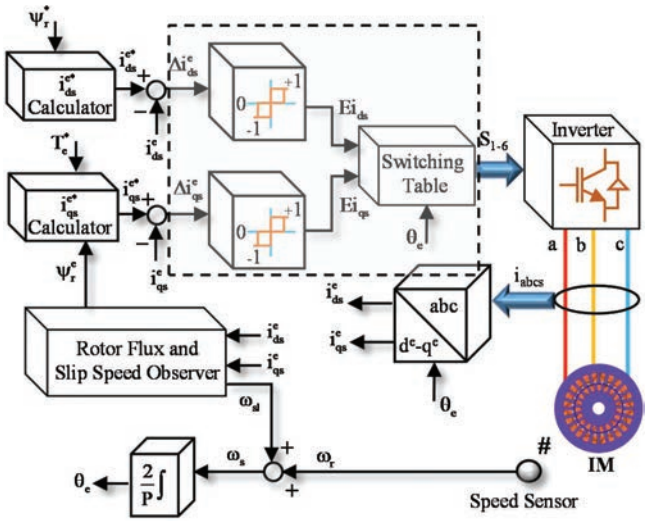

Figure 3 Block diagram of the non-linear field-oriented control algorithm.

which avoids unbalanced phase currents. The DTC structure of this algorithm has also led to high current and torque ripples.

The objective of the proposed DRM-NLFOC scheme is to minimize the RMS q-axis stator current ripple, thereby reducing the electromagnetic torque ripple. To achieve this objective, a new scheme, where the optimal switching duty ratio is computed from the predicted q-axis current response.

In the following section, first, the control principle and conventional control structure of the NLFOC scheme are presented and then the proposed DRM-NLFOC scheme is discussed briefly. In Section 3, a numerical study of the conventional and proposed schemes is elaborated based on the d-axis and q-axis current characteristics, flux characteristics and electromagnetic torque response. The results obtained in the numerical study are also validated experimentally and a brief comparison of results is also presented.

2 Non-Linear Field-Oriented Control Scheme

2.1 Control Principle

The mathematical modelling equations of an induction motor in the synchronous reference frame are expressed as,

$$v_{qs}^{e} = (R_s + L_s\rho)i_{qs}^{e} + \omega_s\psi_{ds}^{e} + L_m\rho i_{qr}^{e} \tag{1}$$

$$v_{ds}^{e} = (R_s + L_s\rho)i_{ds}^{e} - \omega_s\psi_{ds}^{e} + L_m\rho i_{dr}^{e} \tag{2}$$

$$0 = R_r i_{qr}^{e} + \rho\psi_{qr}^{e} + \omega_{sl}\psi_{dr}^{e} \tag{3}$$

$$0 = R_r i_{dr}^{e} + \rho\psi_{dr}^{e} + \omega_{sl}\psi_{qr}^{e} \tag{4}$$

$$\psi_{ds}^{e} = L_m i_{dr}^{e} + L_s i_{ds}^{e} \tag{5}$$

$$\psi_{qs}^{e} = L_m i_{qr}^{e} + L_s i_{qs}^{e} \tag{6}$$

$$\psi_{dr}^{e} = L_m i_{ds}^{e} + L_r i_{dr}^{e} \tag{7}$$

$$\psi_{qr}^{e} = L_m i_{qs}^{e} + L_r i_{qr}^{e} \tag{8}$$

$$T_e = \frac{3}{2}\frac{P}{2}\frac{L_m}{L_r}(\tilde{\psi}_r \times \tilde{i}_s) \tag{9}$$

The objective of the NLFOC scheme is to decouple the electromagnetic torque and the rotor flux linkage (ψ_r) in Equation (9), such that the electromagnetic torque can be independently controlled by the stator q-axis current (i_{qs}^{e}). Therefore, the rotor flux linkage is aligned with its d-axis component (ψ_{dr}^{e}) and held constant in this scheme as expressed in Equation (10) and shown in Figure 4.

$$\psi_{dr}^{e} = \psi_r; \quad \psi_{qr}^{e} = 0 \tag{10}$$

The Equation (9) can be expanded as,

$$T_e = \frac{3}{2}\frac{P}{2}\frac{L_m}{L_r}(\psi_{dr}^{e} i_{qs}^{e} - \psi_{qr}^{e} i_{ds}^{e}) \tag{11}$$

Using Equation (10), Equation (11) reduces to,

$$T_e = \frac{3}{2}\frac{P}{2}\frac{L_m}{L_r}(\psi_r^{e} i_{qs}^{e}) \tag{12}$$

On eliminating rotor current d-q components in the rotor voltage Equations (3)–(4) using Equations (7)–(8),

$$0 = \rho\psi_{qr}^{e} + \frac{R_r}{L_r}\psi_{qr}^{e} - \frac{L_m}{L_r}R_r i_{qs}^{e} + \omega_{sl}\psi_{dr}^{e} \tag{13}$$

$$0 = \rho\psi_{dr}^{e} + \frac{R_r}{L_r}\psi_{dr}^{e} - \frac{L_m}{L_r}R_r i_{ds}^{e} - \omega_{sl}\psi_{qr}^{e} \tag{14}$$

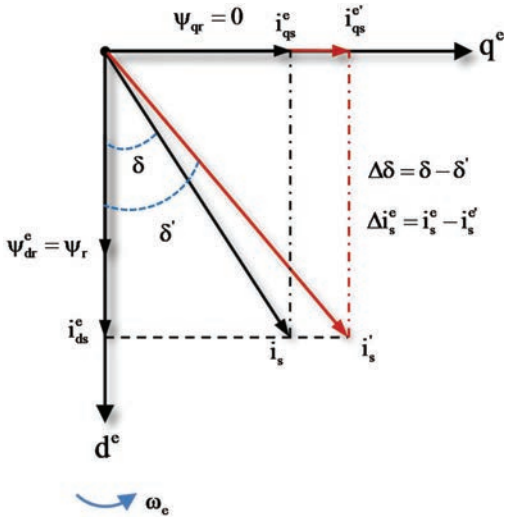

Figure 4 Decoupled stator current control on the electromagnetic torque.

From Equation (10), Equations (13)–(14) becomes,

$$\omega_{sl} = \frac{L_m R_r}{L_r \psi_r} i_{qs} \tag{15}$$

$$\psi_r = L_m i^{e}_{ds} \tag{16}$$

Equation (16) allows the rotor flux to be retained constant using the stator d-axis current component (i^{e}_{ds}). This means that the change in the i^{e}_{qs} current (i^{e}_{qs} to $i^{e'}_{qs}$) (refer to Figure 4) causes a change in the resultant stator current, the angle (δ) between the resultant stator current (i_s) and rotor flux linkage vector (ψ_r). Thus, the electromagnetic torque can be controlled by the i^{e}_{qs} current. The variation in the electromagnetic torque (ΔT_e) (from Equation (9)) can be expressed as,

$$\Delta T_e = \frac{3}{2}\frac{P}{2}\frac{L_m}{L_r}|\psi_r||i_s + \Delta i_s| \sin \Delta\delta \tag{17}$$

2.2 Conventional Control Structure

The block diagram of the NLFOC scheme is shown in Figure 3. The command stator dq-axes current components (i^{e}_{ds} and i^{e}_{qs}) are calculated from the required rotor flux (ψ^{*}_{r}) and the electromagnetic torque (T^{*}_{e}) using

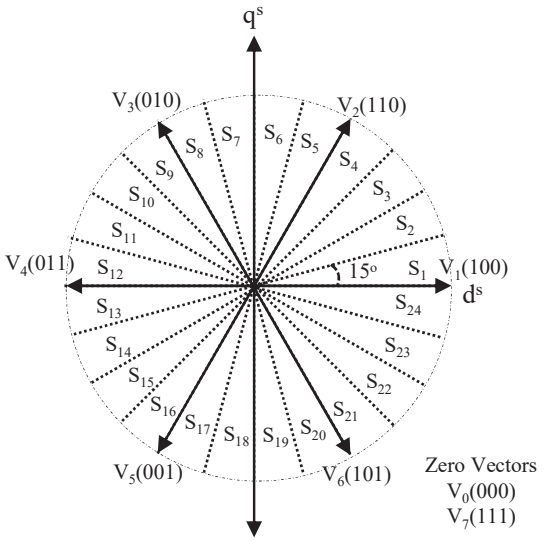

Figure 5 Inverter control voltage vectors (V_0–V_7) and synchronous angle sector (S_1–S_{24}) in stationary d^s-q^s space.

Equations (16) and (12) respectively. The induction motor phase current component errors (Δi^e_{ds} and Δi^e_{qs}) in the synchronous reference frame are fed to the three-level hysteresis controllers. Based on the current error hysteresis level and the synchronous angle sector (S_1–S_{24}) (refer to Figure 5), inverter switching pulses are provided from the switching table (refer to Table 1), to control the induction motor drive.

2.3 A Novel Duty Ratio Modulated NLFOC Scheme

The concept of the duty ratio modulation is to estimate the required switching time of the inverter control pulses. The objective of the proposed duty ratio modulated NLFOC scheme (DRM-NLFOC) is to attain a minimum RMS i^e_{qs} current ripple. Thus, a mathematical equation providing the dependence of the RMS i^e_{qs} current ripple on the duty ratio has to be known. The RMS i^e_{qs} current ripple over a control sampling time (t_{cs}) can be expressed as,

$$i^e_{qs(ripple)} = \sqrt{\frac{1}{t_{cs}} \int_0^{t_{cs}} (i^e_{qs(error)})^2 dt} = \sqrt{\frac{1}{t_{cs}} \int_0^{t_{cs}} (i^e_{qs} - i^{e*}_{qs})^2 dt} \qquad (18)$$

Figure 6 illustrates the steady-state response of the i^e_{qs} current in a control sampling time. It can be noted that the active voltage vector increases the

Table 1 Switching table for NLFOC-IM drive

	Ei_{ds}	+1	+1	+1	0	0	0	−1	−1	−1
Sectors	Ei_{qs}	+1	0	−1	+1	0	−1	+1	0	−1
S_1		V_2	V_1	V_6	V_3	V_0	V_6	V_3	V_4	V_5
S_2		V_2	V_1	V_1	V_3	V_0	V_6	V_4	V_4	V_5
S_3		V_2	V_2	V_1	V_3	V_0	V_6	V_4	V_5	V_5
S_4		V_3	V_2	V_1	V_3	V_0	V_6	V_4	V_5	V_6
S_5		V_3	V_2	V_1	V_4	V_0	V_1	V_4	V_5	V_6
S_6		V_3	V_2	V_2	V_4	V_0	V_1	V_5	V_5	V_6
S_7		V_3	V_3	V_2	V_4	V_0	V_1	V_5	V_6	V_6
S_8		V_4	V_3	V_2	V_4	V_0	V_1	V_5	V_6	V_1
S_9		V_4	V_3	V_2	V_5	V_0	V_2	V_5	V_6	V_1
S_{10}		V_4	V_3	V_3	V_5	V_0	V_2	V_6	V_6	V_1
S_{11}		V_4	V_4	V_3	V_5	V_0	V_2	V_6	V_1	V_1
S_{12}		V_5	V_4	V_3	V_5	V_0	V_2	V_6	V_1	V_2
S_{13}		V_5	V_4	V_3	V_6	V_0	V_3	V_6	V_1	V_2
S_{14}		V_5	V_4	V_4	V_6	V_0	V_3	V_1	V_1	V_2
S_{15}		V_5	V_5	V_4	V_6	V_0	V_3	V_1	V_2	V_2
S_{16}		V_6	V_5	V_4	V_6	V_0	V_3	V_1	V_2	V_3
S_{17}		V_6	V_5	V_4	V_1	V_0	V_4	V_1	V_2	V_3
S_{18}		V_6	V_5	V_5	V_1	V_0	V_4	V_2	V_2	V_3
S_{19}		V_6	V_6	V_5	V_1	V_0	V_4	V_2	V_3	V_3
S_{20}		V_1	V_6	V_5	V_1	V_0	V_4	V_2	V_3	V_4
S_{21}		V_1	V_6	V_5	V_2	V_0	V_5	V_2	V_3	V_4
S_{22}		V_1	V_6	V_6	V_2	V_0	V_5	V_3	V_3	V_4
S_{23}		V_1	V_1	V_6	V_2	V_0	V_5	V_3	V_4	V_4
S_{24}		V_2	V_1	V_6	V_2	V_0	V_5	V_3	V_4	V_5

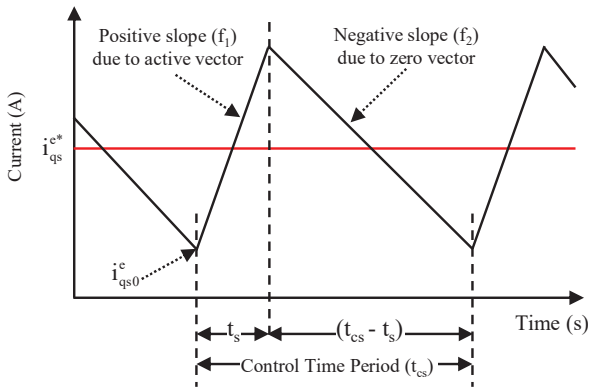

Figure 6 Response of the q-axis Stator Current Over the Control Sampling Time, t_{cs}.

i^e_{qs} current in time $0 - t_s$ (positive slope, f_1), while the zero voltage vector reduces the i^e_{qs} current in time $t_{cs} - t_s$ (negative slope, f_2). If i^e_{qso} is the initial i^e_{qs} current, the positive and negative slope intervals (from Figure 6) can be expressed as,

$$i^e_{qs} = \begin{cases} i^e_{qso} + f_1 t, & 0 \le t \le t_s \\ i^e_{qso} + f_1 t_s + f_2 t - f_2 t_s, & t_s \le t \le t_{cs} \end{cases} \tag{19}$$

Using Equation (19), Equation (18) can be expanded as,

$$i^e_{qs(ripple)} = \sqrt{\frac{1}{t_{cs}}\left[\int_0^{t_s} (i^e_{qso} + f_1 t - i^{e*}_{qs})^2 dt\right]} + \sqrt{\frac{1}{t_{cs}}\int_{t_s}^{t_{cs}} (i^e_{qso} + f_1 t_s + f_2 t - f_2 t_s - i^{e*}_{qs})^2 dt} \tag{20}$$

To achieve minimum i^e_{qs} ripple, the following condition has to be satisfied (from the calculus maxima and minima principle).

$$\frac{\partial i^e_{qs(ripple)}}{\partial t_s} = 0 \tag{21}$$

Equations (20)–(21) have to be solved to establish the mathematical relation between RMS i^e_{qs} current ripple and switching time (t_s) to achieve minimum ripple condition. To solve these equations, slopes f_1 and f_2 have to be known and can be derived from the induction motor modelling Equations (1)–(19).

The v^e_{qs} voltage Equation (1) can be expressed in terms of i^e_{qs} and stator-rotor flux linkages using Equation (8) as,

$$v^e_{qs} = \frac{L_m}{L_r}\rho\psi^e_{qr} + R_s i^e_{qs} + \sigma L_s \rho i^e_{qs} + \omega_s \psi^e_{ds} \tag{22}$$

Where, $\sigma = \left[1 - \frac{L_m^2}{L_s L_r}\right]$

On rearranging Equation (22),

$$\rho\psi^e_{qr} = \frac{L_r}{L_m} v^e_{qs} - \frac{L_r R_s}{L_m} i^e_{qs} - \frac{\sigma L_s L_r}{L_m}\rho i^e_{qs} - \frac{L_r}{L_m}\omega_s \psi^e_{ds} \tag{23}$$

Similarly, from Equation (13),

$$\rho\psi^e_{qr} = \frac{R_r L_m}{L_r} i^e_{qs} - \frac{R_r}{L_r}\psi^e_{qr} - \omega_{sl}\psi^e_{dr} \tag{24}$$

The Equations (23) and (24) are solved and simplified to express the rate of change of i^e_{qs} as,

$$\rho i^e_{qs} = Av^e_{qs} - Bi^e_{qs} - A\omega_s \psi^e_{ds} + \frac{R_r L_m}{\sigma L_s L_r^2}\psi^e_{qr} + C\omega_{sl}\psi^e_{dr} \tag{25}$$

Where, $A = \frac{1}{\sigma L_s}$, $B = \frac{L_r^2 R_s + R_r L_m^2}{\sigma L_s L_r^2}$, $C = \frac{L_m}{\sigma L_s L_r}$

Using Equation (7), Equation (5) can be rewritten as,

$$\psi^e_{ds} = \frac{L_m}{L_r^2}\psi^e_{dr} - \left[\frac{L_m^2 - L_s L_r}{L_r^2}\right] i^e_{ds} \tag{26}$$

Eliminate ψ^e_{ds} from Equation (25) using Equation (26),

$$\rho i^e_{qs} = \left[Av^e_{qs} - Bi^e_{qs} + \frac{R_r L_m}{\sigma L_s L_r^2}\psi^e_{qr} + D\omega_s i^e_{ds} - [E\omega_s - C\omega_{sl}]\psi^e_{dr}\right] \tag{27}$$

Where, $D = A\left[\frac{L_m^2 - L_s L_r}{L_r^2}\right]$, $E = A\frac{L_m}{L_r^2}$

On applying the decoupled electromagnetic torque control condition (from Equation (10)), Equation (27) becomes,

$$\rho i^e_{qs} = Av^e_{qs} - Bi^e_{qs} + D\omega_s i^e_{ds} - [E\omega_s - C\omega_{sl}]\psi_r \tag{28}$$

For a small sampling period t_{sp}, Equation (28) can be represented as,

$$\rho i^e_{qs} = \frac{\Delta i^e_{qs}}{t_{sp}} = [Av^e_{qs} - Bi^e_{qs} + D\omega_s i^e_{ds} - [E\omega_s - C\omega_{sl}]\psi_r] \tag{29}$$

Thus, positive and negative slopes of the i^e_{qs} current are found to be,

$$f_1 = \frac{\Delta i^e_{qs}}{t_{sp}} = [Av^e_{qs} - Bi^e_{qs} + D\omega_s i^e_{ds} - [E\omega_s - C\omega_{sl}]\,\psi_r] \tag{30}$$

$$f_2 = \frac{\Delta i^e_{qs}}{t_{sp}} = [-Bi^e_{qs} + D\omega_s i^e_{ds} - [E\omega_s - C\omega_{sl}]\,\psi_r] \tag{31}$$

By substituting slope Equations (30)–(31) in Equation (20), the RMS i^e_{qs} current ripple is calculated and partially differentiated to satisfy the minimum ripple condition (Equation (21)) [34].

$$\frac{\partial i^e_{qs(ripple)}}{\partial t_s} = \sqrt{-\frac{(f_1 - f_2)}{t_{cs}}\begin{bmatrix}(2f_1 - f_2)t_s^2 \\ \quad + 2(i^e_{qso} - i^{e*}_{qs} - (f_1 - f_2)t_{cs})t_s \\ \quad - (2(i^e_{qso} - i^{e*}_{qs})t_{cs} + f_2 t_{cs}^2)\end{bmatrix}} = 0 \tag{32}$$

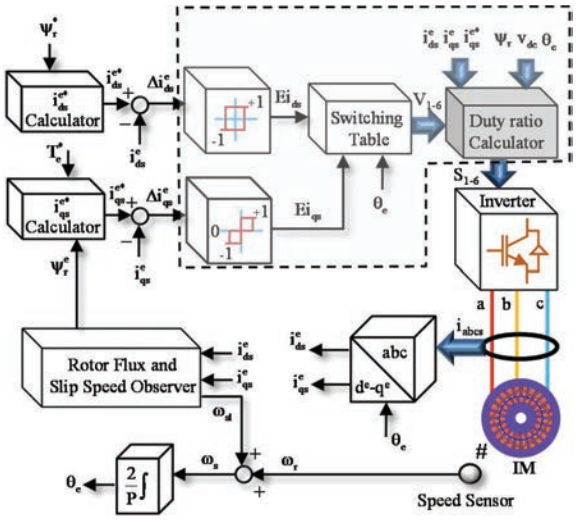

Figure 7 Block diagram of the DRM-NLFOC scheme.

The Equation (32) is solved to find the optimal active vector switching time (t_s) [35].

$$t_s = \frac{2(i_{qs}^{e*} - i_{qso}^{e}) - f_2 t_{cs}}{2f_1 - f_2} \tag{33}$$

This equation is resolved to calculate the optimal switching time in the duty ratio calculator block of the proposed DRM-NLFOC scheme (shown in Figure 7). The implementation flow chart of this block is highlighted in Figure 8.

Here a two-level and three-level hysteresis band are used for both i_{ds}^{e} and i_{qs}^{e} error controllers respectively. The space vector representation of the control voltage vectors and the switching table for this scheme are given in Figure 9 and Table 2 respectively.

3 Results and Discussion

The efficacy of the proposed DRM-NLFOC scheme is investigated numerically and validated experimentally. The numerical study has been carried out using MATLAB/Simulink. Table 3 provides the specifications and equivalent circuit parameters of the test induction motor. The control execution flowcharts, adopted for the NLFOC and DRM-NLFOC schemes for the

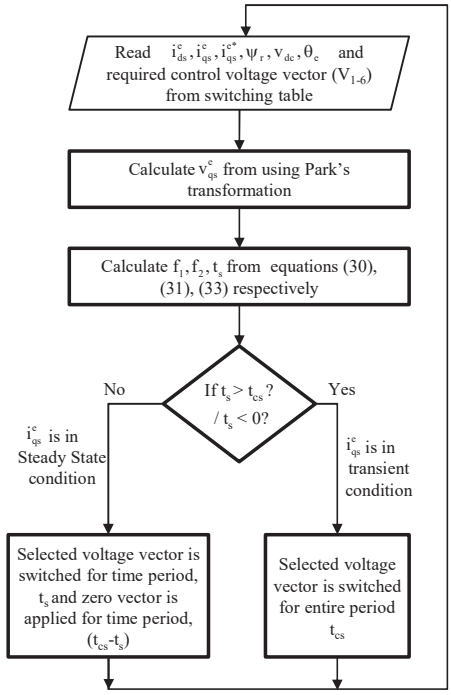

Figure 8 Implementation flowchart of the duty-ratio calculator block.

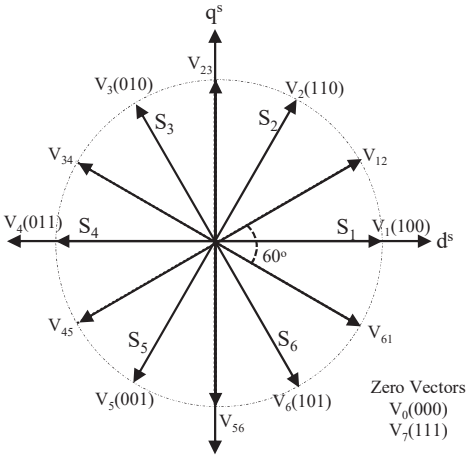

Figure 9 Space vector representation of active voltage vectors in 6 sectors.

Table 2 Switching table for DRM-NLFOC drive

		Sectors					
Ei_{ds}	Ei_{qs}	S_1	S_2	S_3	S_4	S_5	S_6
+1	$+1$	V_2	V_3	V_4	V_5	V_6	V_1
	0	V_7	V_0	V_7	V_0	V_7	V_0
	-1	V_6	V_1	V_2	V_3	V_4	V_5
-1	$+1$	V_3	V_4	V_5	V_6	V_1	V_2
	0	V_0	V_7	V_0	V_7	V_0	V_7
	-1	V_5	V_6	V_1	V_2	V_3	V_4

Table 3 Specifications and equivalent circuit parameters of a 1 kW, 3-phase induction motor

Specifications/Parameters	Values
Rated speed	713 rpm
Rated DC-link voltage	72 V
No. of pole pairs	4
Stator phase resistance	0.209 Ω
Stator phase leakage-inductance	1.19 mH
Rotor phase resistance	0.185 Ω
Rotor phase leakage-inductance	2.24 mH
Magnetizing inductance	10.6 mH
Rated stator flux linkage	0.2 Wb
Rated rotor flux linkage	0.17 Wb

numerical and experimental analysis are shown in Figure 10. The test conditions adopted for these analyses are as follows,

- Fundamental sampling time – 20 μs
- i^e_{ds} and i^e_{qs} error hysteresis bandwidth – 0.05 A
- Control sampling time – 200 μs

3.1 Numerical Study

The induction motor drive performance, due to NLFOC and DRM-NLFOC schemes at 713 rpm and 300 rpm are depicted in Figures 11–12 respectively. Since the i^e_{ds} current and i^e_{qs} current ripples directly impact the electromagnetic torque (refer Equation (12)), rotor flux (refer Equation (16)) and stator current THD, the characteristics of these components at various drive speed-load conditions are consolidated graphically and presented in Figure 13.

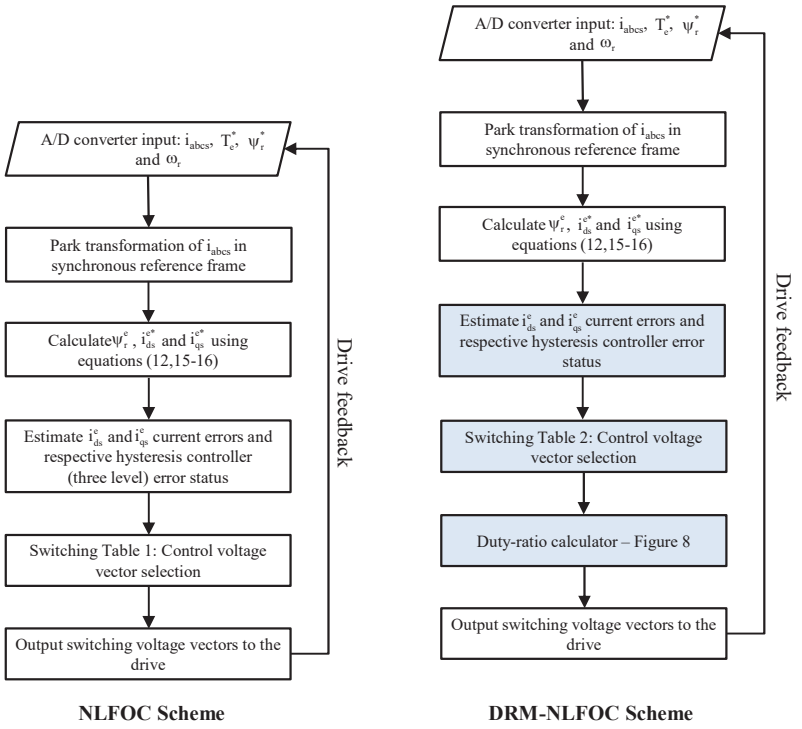

Figure 10 Control execution flow chart of the NLFOC and DRM-NLFOC scheme.

Analysis of the d-axis and q-axis Current Ripple

In NLFOC drives, the steady-state response of the i_{ds}^e and i_{qs}^e currents depends on the stator and rotor time constants [7, 8]. The large rotor time constant of the induction motor drive leads to a slower i_{ds}^e current response. Whereas, the i_{qs}^e current has a quicker response to the inverter switching vector because of the small stator time constant. Thus, limiting the i_{qs}^e current error within the hysteresis band has been a challenge and causes a high ripple. However, the switching of the inverter at the appropriate duty ratio in the DRM-NLFOC scheme has led to a reduction in current ripples.

The i_{ds}^e i_{qs}^e current ripples are reduced by 82.24% and 88.13% respectively (as shown in Figure 13) at 713 rpm. The d-q axes current component ripples distort the stator current waveform. Thus, the reduction in the stator current ripples in DRM-NLFOC has also improved the profile of the stator current waveform compared to the NLFOC scheme and resulted in the stator current THD of 0.22% (from Figure 13).

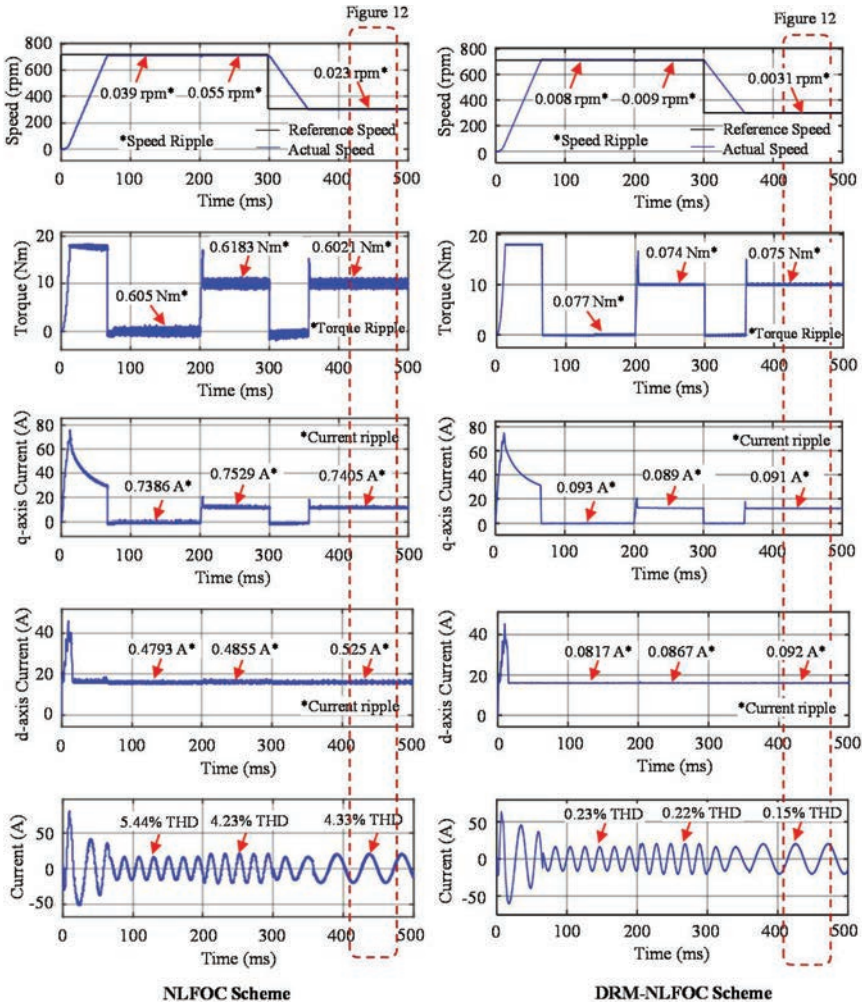

Figure 11 Induction motor drive performance based on NLFOC and DRM-NLFOC schemes – electromagnetic torque and stator current response.

Flux Characteristics

From the NLFOC principle, it is evident that the rotor flux is indirectly controlled by the i_{ds}^{e} current (refer to Equation (16)). With the reduction in the d-axis current ripple, the rotor flux ripple has been observed to be 0.0001 Wb in the DRM-NLFOC scheme, which is about 93.75% lower than the NLFOC scheme at a drive speed of 713 rpm and 10 Nm load.

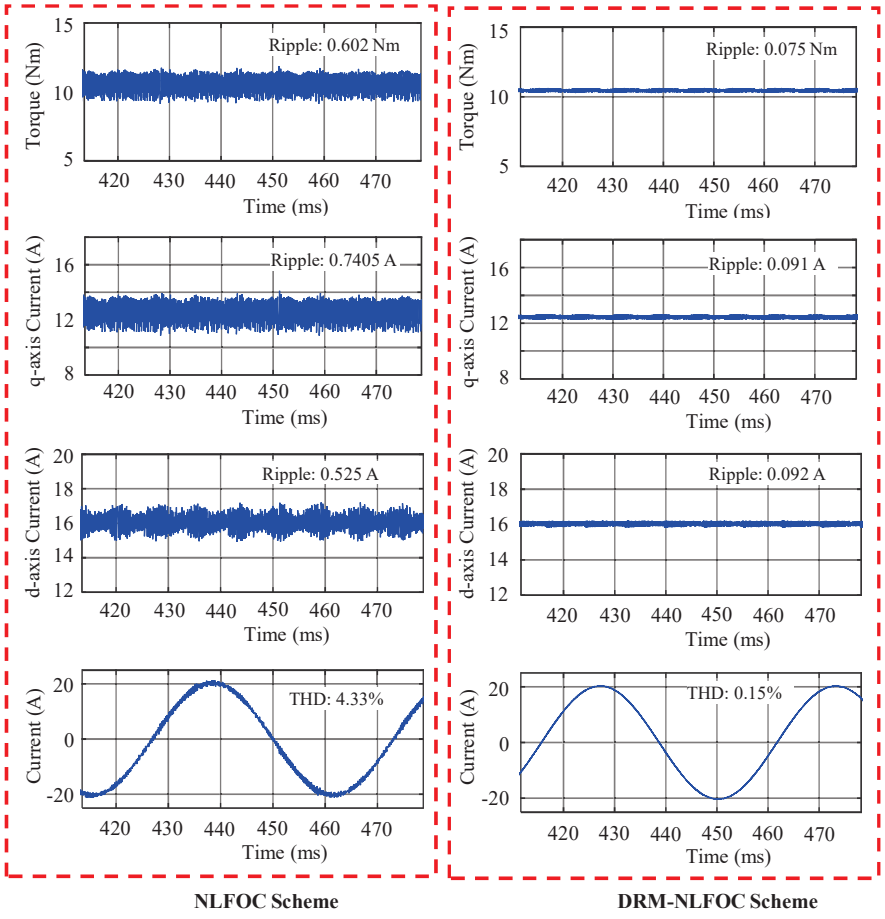

Figure 12 Steady state drive characteristics – electromagnetic torque and stator current components.

Electromagnetic Torque Response

In steady-state, the electromagnetic torque response is a function of the i_{qs}^{e} current and rotor flux characteristics (as seen in Equation (12)). In the DRM-NLFOC scheme, the duty ratio of the control voltage vector is calculated prior, to ensure minimum RMS i_{qs}^{e} current ripple. This has led to a decrease in the i_{qs}^{e} current ripple and also caused the electromagnetic torque ripple to reduce by about 88% compared to the NLFOC scheme at 713 rpm and 10 Nm load (as shown in Figure 13).

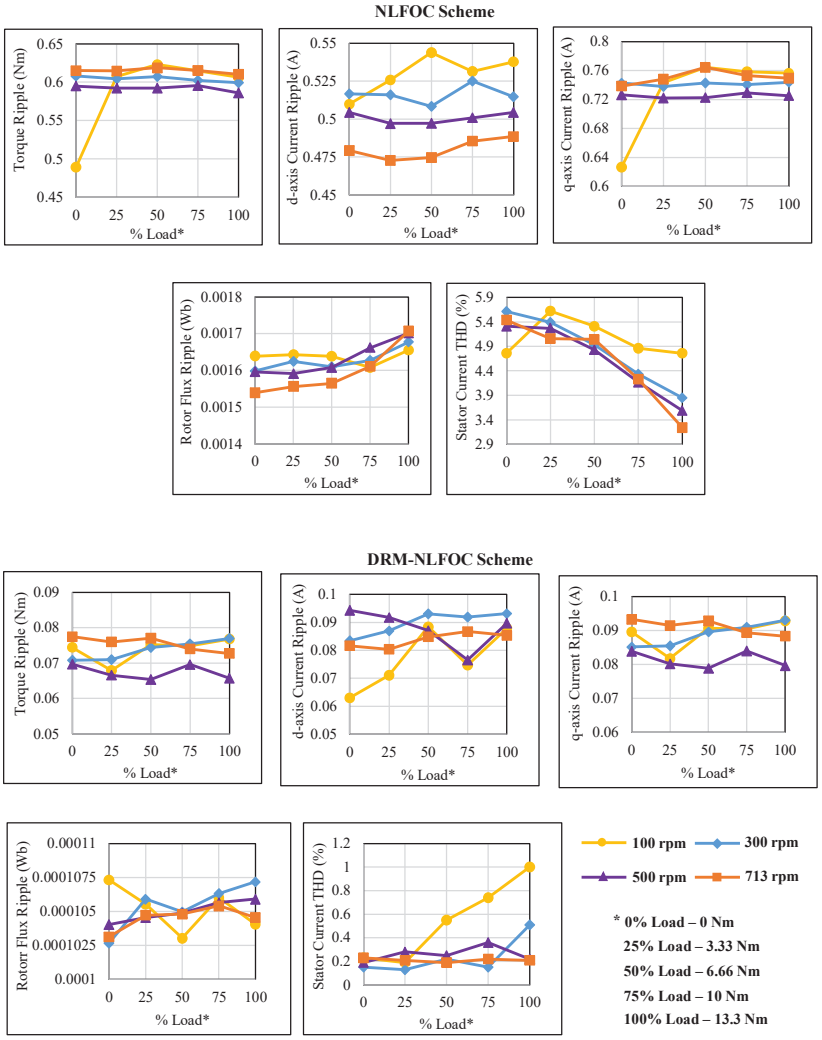

Figure 13 Numerical study – NLFOC and DRM-NLFOC based induction motor drive characteristics at various drive speeds and load conditions.

3.2 Experimental Validation

The experimental test setup is shown in Figure 14 and consists of the following components,

- Motor test-bed – 1 kW induction motor (test) coupled with 3.7 kW DC generator (load)

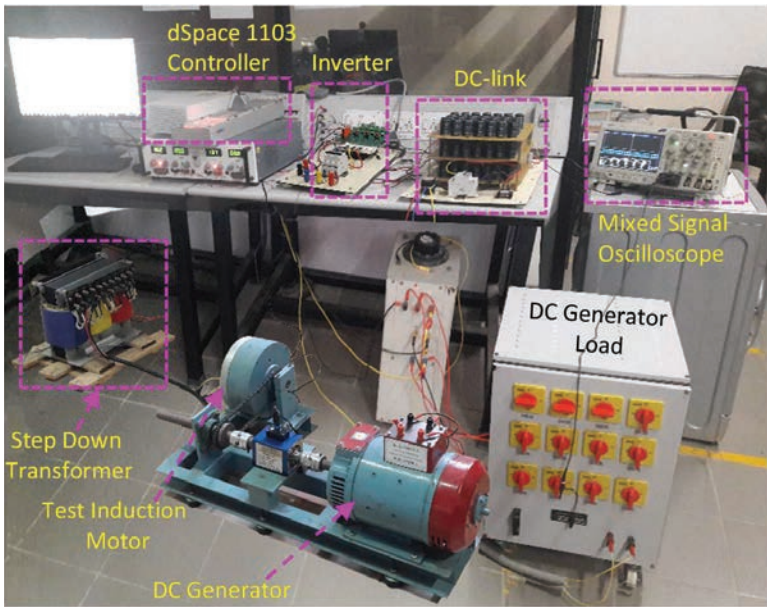

Figure 14 Experimental test setup.

- Controller – The control schemes are executed using the dSpace 1103 controller
- Power inverter drive unit – Three-phase inverter IGBT module, Infineon FS100R06KE3 driven by IR2110 driver circuits with 10 μs dead time. Bidirectional current sensor ACS758 is used to measure inverter phase current

Figures 15 and 16 shows the steady-state stator current and electromagnetic torque responses of the NLFOC and DRM-NLFOC based induction motor drives respectively at rated drive speed (713 rpm). The drive performance has been presented for both no-load and 10 Nm load conditions. Similar to the numerical study, the effects of the current and current characteristics on various drive components are analysed and depicted graphically in Figure 17.

The experiment results observed in Figures 15–17 resemble numerical study, irrespective of the real-time constraints such as signal delay, sensor offsets/errors, machine dynamics etc. Thus, proving the efficacy of the proposed algorithm. A summary of the drive performance due to NLFOC and DRM- NLFOC schemes at various speeds is presented in Table 4.

Table 4 Performance comparison of 1 kW induction motor drive: NLFOC scheme and DRM-NLFOC scheme

Performance Parameter		300 rpm 10 Nm Load			713 rpm 10 Nm Load		
		NLFOC Scheme	DRM-NLFOC Scheme	Difference % (Compared to NLFOC Scheme)	NLFOC Scheme	DRM-NLFOC Scheme	Difference % (Compared to NLFOC Scheme)
q-axis current ripple	Simulation Result	0.74A	0.09A	87.84% ↓	0.75A	0.089A	88.13% ↓
	Experimental Result	0.95A	0.24A	74.74% ↓	0.97A	0.24A	75.26% ↓
Electromagnetic Torque ripple	Simulation Result	0.6Nm	0.075Nm	87.5% ↓	0.61Nm	0.074Nm	87.87% ↓
	Experimental Result	0.78Nm	0.21Nm	73.08% ↓	0.8Nm	0.19Nm	76.25% ↓
d-axis current ripple	Simulation Result	0.53A	0.09A	83.02% ↓	0.49A	0.087A	82.24% ↓
	Experimental Result	0.64A	0.21A	67.19% ↓	0.59A	0.2A	66.1% ↓
Stator current harmonics	Simulation Result	4.33%	0.15%	96.53% ↓	4.23%	0.22%	94.8% ↓
	Experimental Result	5.34%	1.62%	69.66% ↓	5.32%	1.6%	69.92% ↓
Rotor flux ripple	Simulation Result	1.6mWb	0.1mWb	93.75% ↓	1.6mWb	0.1mWb	93.75% ↓
	Experimental Result	2.1mWb	0.37mWb	82.38% ↓	2mWb	0.37mWb	81.5% ↓

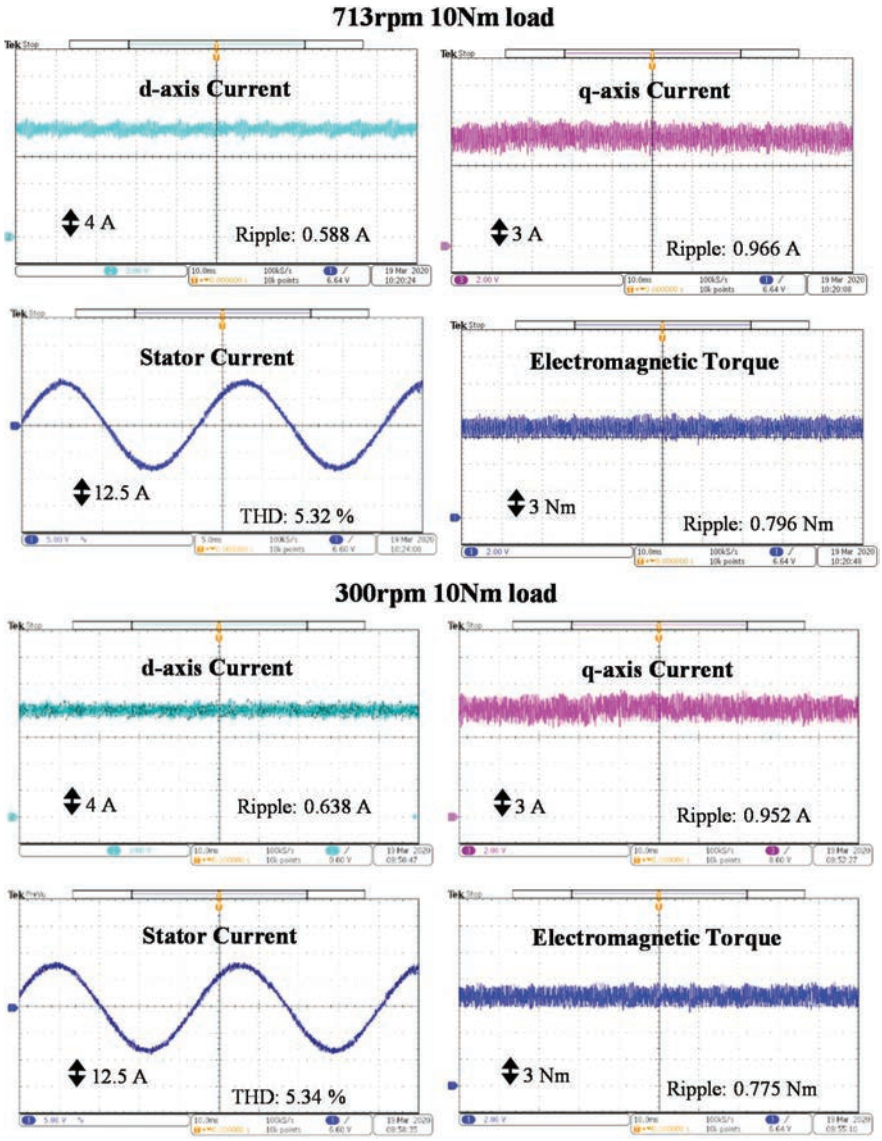

Figure 15 NLFOC based induction motor drive – steady state performance at 713 rpm and 300 rpm.

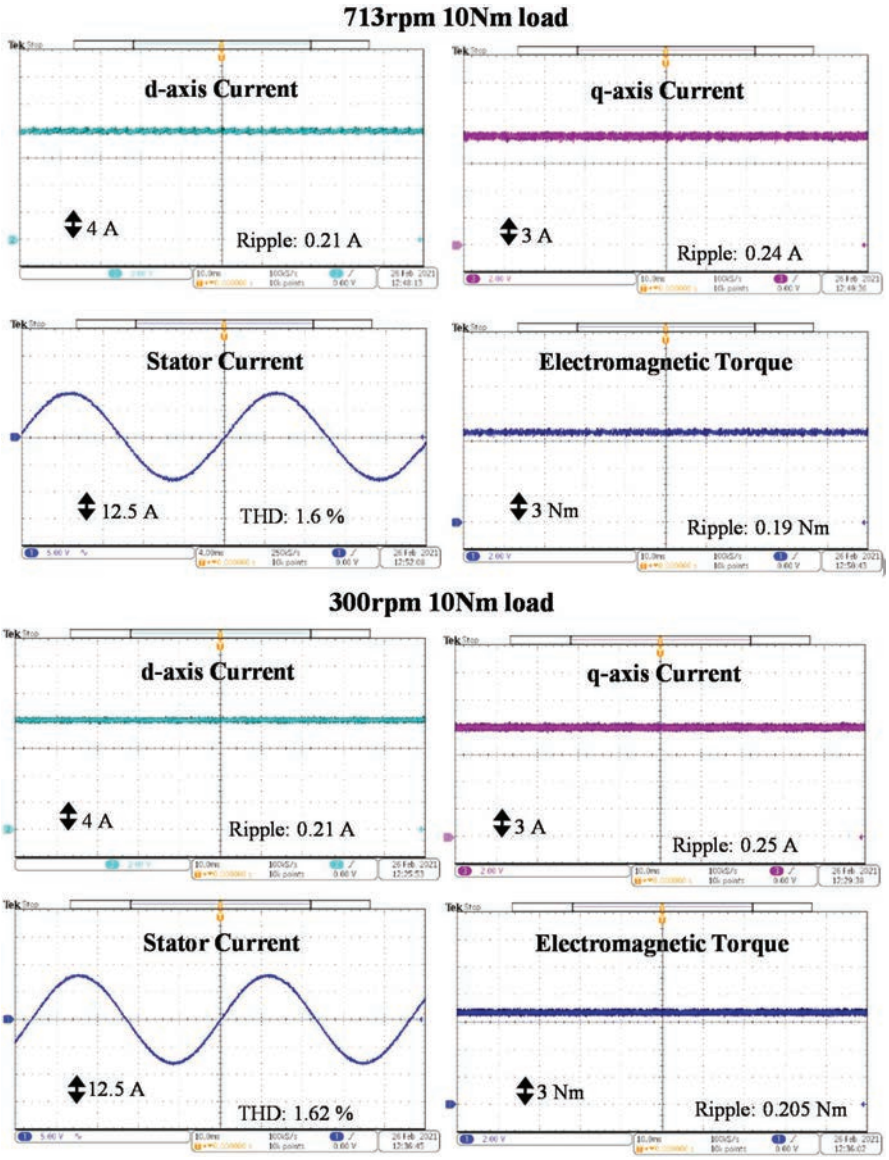

Figure 16 DRM-NLFOC based induction motor drive – steady state performance at 713 rpm and 300 rpm.

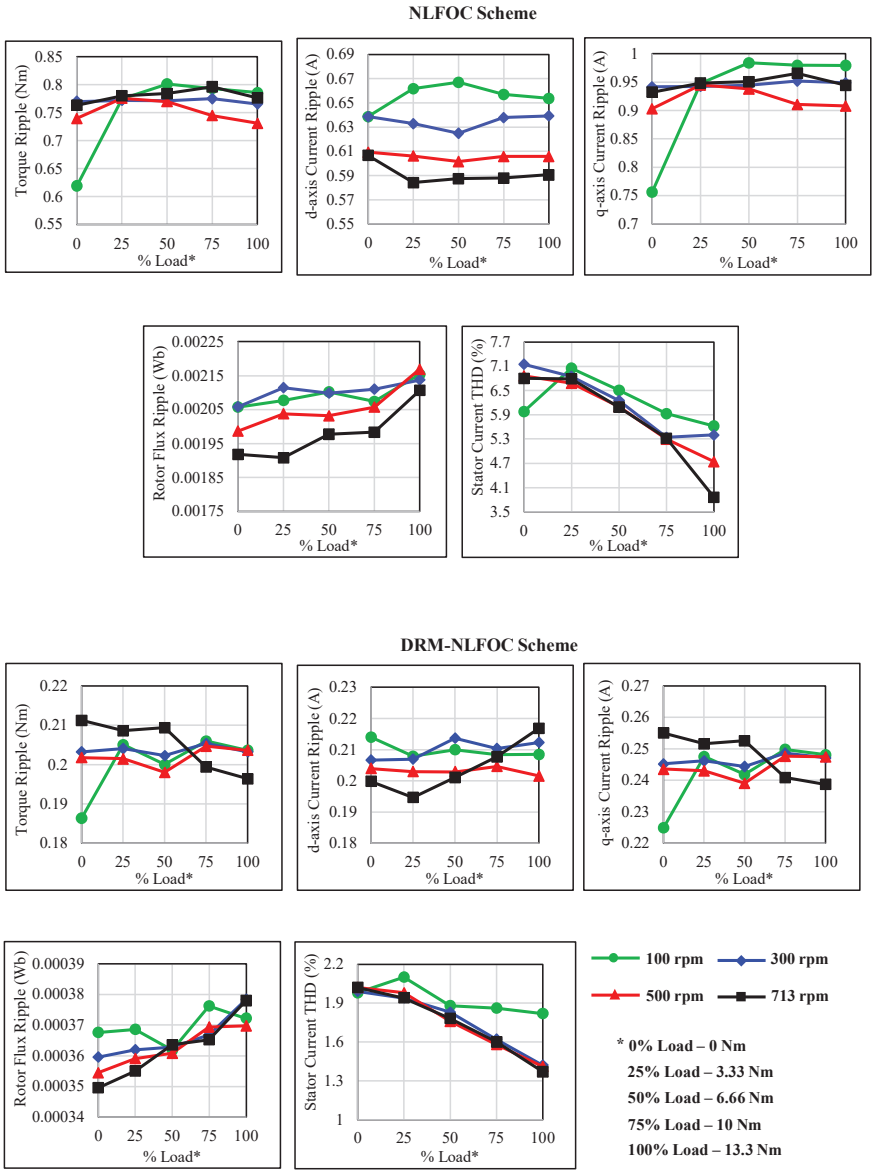

Figure 17 Experimental study – NLFOC and DRM-NLFOC based induction motor drive characteristics at various drive speeds and load conditions.

4 Conclusions

In this paper, duty ratio control of the space vector has been incorporated into the NLFOC scheme. The objective of the duty ratio control has been to obtain a minimum RMS q-axis current ripple. From the results following observations can be made,

- The d-q axes current ripple has been reported to be reduced by 66.64% and 75% (average) respectively (refer to Table 4).
- The reduction in the current component ripples has led to a decrease in the electromagnetic torque ripple and stator current THD by 74.67% and 69.79% (average) respectively (refer to Table 4).

Furthermore, the DRM- NLFOC scheme modulates the inverter control voltage vector at a constant switching frequency compared to the NLFOC scheme. The thermal impact and ageing of the motor drive can cause parameter variation and may result in an error while calculating the required duty ratio. To overcome this, parameters error compensation techniques such as using the Kalman Filter, least-square estimation etc. can be applied.

References

[1] Bose B K, 'Modern Power Electronics and AC Drives', PHI Learning Pvt. Ltd, 2002.
[2] Krishnan R, 'Electric Motor Drives: Modeling, Analysis, and Control', Prentice-Hall, 2001.
[3] Husain M A, Rajput R, Gupta M K, Tabrez M, Ahmad M W, Bakhsh F I (2022) Design and implementation of different drive topologies for control of induction motor for electric vehicle application. Distributed Generation & Alternative Energy Journal 37:999–1026.
[4] Blaschke F (1971) A new method for the structural decoupling of A.C. induction machines. Conf. Rec. IFAC. Duesseldorf, Germany, 1971, 1–15.
[5] Kazmierkowski M P, Malesani L (1998) Current control techniques for three-phase voltage-source PWM converters: a survey. IEEE Transactions on Industrial Electronics 45:691–703.
[6] Holmes D G, McGrath B P, Parker S G (2012) Current regulation strategies for vector-controlled induction motor drives. IEEE Transactions on Industrial Electronics 59:3680–3689.

[7] Lee D C, Sul S K, Park M H (1994) High performance current regulator for a field-oriented controlled induction motor drive. IEEE Transactions on Industry Applications 30:1247–1257.
[8] Singh G K, Singh D K P, Nam K, Lim S K (2005) A simple indirect field-oriented control scheme for multiconverter-fed induction motor. IEEE Transactions on Industrial Electronics 52:1653–1659.
[9] Wang K, Li Y, Ge Q, Shi L (2018) An improved indirect field-oriented control scheme for linear induction motor traction drives. IEEE Transactions on Industrial Electronics 65:9928–9937.
[10] Holmes D G, Lipo T A, McGrath B P, Kong W Y (2009) Optimized design of stationary frame three phase ac current regulators. IEEE Transactions on Power Electronics 24:2417–2426.
[11] Domínguez J R, Dueñas I, Ortega-Cisneros S (2020) Discrete-time modeling and control based on field orientation for induction motors. IEEE Transactions on Power Electronics 35:8779–8793.
[12] Jain J K, Ghosh S, Maity S (2020) concurrent pi controller design for indirect vector controlled induction motor. Asian Journal of Control 22:130–142.
[13] Rezgui S E, Benalla H (2013) New robust and mechanical sensorless scheme for SVM inverter fed induction motor drive using variable structure controllers and MRAS. Arabian Journal of Science and Engineering 38:1449–1458.
[14] Hannan M A, Ali J A, Mohamed A, Amirulddin U A U, Tan N M L, Uddin M N (2018) Quantum-behaved lightning search algorithm to improve indirect field-oriented fuzzy-pi control for IM drive. IEEE Transactions on Industry Applications 54:3793–3805.
[15] Dalal Zellouma, Youcef Bekakra, Habib Benbouhenni (2023) Field-oriented control based on parallel proportional–integral controllers of induction motor drive. Energy Reports 9:4846-4860.
[16] Brod D M, Novotny D W (1985) Current control of VSI-PWM inverters. IEEE Transactions on Industry Applications IA-21:562–570.
[17] Kazmierkowski M P, Dzieniakowski M A, Sulkowski W (1991) Novel space vector based current controllers for PWM-inverters. IEEE Transactions on Power Electronics 6:158–166.
[18] Kazmierkowski M P, Sulkowski W (1991) A novel vector control scheme for transistor PWM inverter-fed induction motor drive. IEEE Transactions on Industrial Electronics 38:41–47.

[19] Pan C T, Chang T Y (1994) An improved hysteresis current controller for reducing switching frequency. IEEE Transactions on Power Electronics 9:97–104.
[20] Yi-Hwa Liu, Chern-Lin Chen, Rong-Jie Tu (1998) A novel space-vector current regulation scheme for a field-oriented-controlled induction motor drive. IEEE Transactions on Industrial Electronics 45:730–737.
[21] Kwon B H, Kim T W, Youn J H (1998) A novel SVM-based hysteresis current controller. IEEE Transactions on Power Electronics 13:297–307.
[22] Vaez-Zadeh S, Jalali E (2007) Combined vector control and direct torque control method for high performance induction motor drives. Energy Conversion and Management 48:3095–3101.
[23] Hemantha Kumar R, Lenin N C (2021) Current ripple reduction to improve electromagnetic torque and flux characteristics in AC drives, International Journal of Electronics. 109:1421–1442.
[24] Feraga C E, Sedraoui M, Bachir Bouiadjra R (2019) Enhanced indirect field-oriented control of single-phase induction motor drive using H8 current controller. Arabian Journal of Science and Engineering 44: 7187–7202.
[25] Kawamura A, Hoft R G (1984) Instantaneous feedback controlled PWM inverters with adaptive hysteresis. IEEE Transactions on Industry Applications IA-20:769–775.
[26] Bose B K (1990) An adaptive hysteresis-band current control technique of a voltage-fed PWM inverter for machine drive system. IEEE Transactions on Industrial Electronics 37:402–408.
[27] Holtz J, Beyer B (1994) The trajectory tracking approach-a new method for minimum distortion PWM in dynamic high-power drives. IEEE Transactions on Industry Applications 30:1048–1057.
[28] El-Sayed I F (1997) Rotor-field orientation with optimal torque-control strategy for current-fed induction-machine system. European Transactions on Electrical Power 7:269–274.
[29] Wang S Y, Tseng C L, Chiu C J (2015) online speed controller scheme using adaptive supervisory tsk-fuzzy cmac for vector controlled induction motor drive. Asian Journal of Control 17:569–581.
[30] Beltran-Carbajal F, Tapia-Olvera R, Valderrabano-Gonzalez A, Lopez-Garcia I (2021) Adaptive neuronal induction motor control with an 84-pulse voltage source converter. Asian Journal of Control 23:1603–1616.
[31] Takahashi I, Noguchi T (1986) A new quick-response and high-efficiency control strategy of an induction motor. IEEE Transactions on Industry Applications IA-22:820–827.

[32] Takahashi I, Ohmori Y (1989) High-performance direct torque control of an induction motor. IEEE Transactions on Industry Applications 25:257–264.
[33] Kumar R H, Iqbal A, Lenin N C (2018) Review of recent advancements of direct torque control in induction motor drives – a decade of progress. IET Power Electronics 11:1–15.
[34] Buja G S, Kazmierkowski M P (2004) Direct torque control of PWM inverter-fed AC motors – a survey. IEEE Transactions on Industrial Electronics 51:744–757.
[35] Kang J K, Sul S K (1999) New direct torque control of induction motor for minimum torque ripple and constant switching frequency. IEEE Transactions on Industry Applications 35:1076–1082.
[36] Casadei D, Profumo F, Serra G, Tani A (2002) FOC and DTC: Two viable schemes for induction motors torque control. IEEE Transactions on Power Electronics 17:779–787.
[37] Sampath Kumar S, Joseph Xavier R, Balamurugan S (2022) Fuzzy-based estimation of reference flux, reference torque and sector rotation for performance improvement of DTC-IM drive. Automatika 63: 440–453.
[38] Çavuş B, Aktaş M (2023) MPC-based flux weakening control for induction motor drive with DTC for electric vehicles. IEEE Transactions on Power Electronics 38:4430–4439.
[39] Najib El Ouanjli N E, Said Mahfoud, Ameena Saad Al-Sumaiti, Soukaina El Daoudi, Aziz Derouich, Mohammed El Mahfoud, Mahmoud A. Mossa (2023) Improved twelve sectors DTC strategy of induction motor drive using backstepping speed controller and P-MRAS stator resistance identification-design and validation. Alexandria Engineering Journal 80:358–371.

Biographies

Hemantha Kumar Ravi is pursuing PhD at Vellore Institute of Technology, Chennai, India. He has received a grant from the Institution of Engineers (India) for the development of the 1 kW direct torque-controlled induction motor drive. He has also been involved in a project funded by the Combat Vehicles Research Development Establishment (CVRDE), DRDO India as a Junior Research Fellow. During the project, he designed (a) control algorithms for electrical generators such as (i) induction generators,

(ii) permanent magnet synchronous generators, (iii) synchronous reluctance generators and (b) DC-DC converters for solar and battery charging applications. He has published 7 international journals and 5 international conferences. His research areas are in the vector control of AC drives for automotive applications.

Sathyanarayanan Nandagopal is a PhD research scholar with the School of Electrical Engineering, Vellore Institute of Technology, Chennai, India. He worked as a Junior Research Fellow (JRF) at Vellore Institute of Technology, Chennai, India for Combat Vehicles Research and Development Establishment (CVRDE), Defence Research and Development Organisation (DRDO), India. During this period he designed and analysed single-phase and three-phase induction generators. His research interests include the design and analysis of induction motors in the hub and frame mount for electric two-wheelers and three-wheelers with a power range of 1 kW to 5 kW. Further to this, his interests include domestic applications such as ceiling fans, IE4 efficiency motors for mono-block and submersible pumps in the range of 4 kW to 11 kW. He has published 6 journal articles and has presented at various conferences including SAE ADMMS'19 and ITEC India 2019.

Lenin Natesan Chokkalingam completed his PhD at Anna University, Chennai in the year 2012. He has published more than 50 international journals and international conferences. He is involved in various consultancy and funded projects for developing high-performance electric motor drives. He has four patents. He serves as an editor and associate editor in "The Global Electrical Engineers" and "International Journal of Electrical and Computer Engineering" respectively. He is an editorial member of the Majlesi Journal of Energy Management. He has 19 years of teaching experience. Currently, he is working as a Professor and Deputy Director in the Electric Vehicles – Incubation, Testing and Research Centre, Vellore Institute of Technology, Chennai, India. His areas of interest are finite element analysis, advanced electromagnetics, design of low-cost, high-performance electrical machines and their controllers for automotive and domestic applications.